




Critical Velocity Ionization in Substellar Atmospheres

A. D. Wilson¹ , I. Dobbs-Dixon², D. A. Diver¹, and C. R. Stark³¹ School of Physics and Astronomy, Kelvin Building, University of Glasgow, Glasgow, G12 8QQ, UK; aldasair.wilson@glasgow.ac.uk² Department of Physics, New York University Abu Dhabi, PO Box 129188 Abu Dhabi, UAE³ Division of Computing and Mathematics, Abertay University, Dundee, DD1 1HG, UK

Received 2019 October 10; revised 2019 November 13; accepted 2019 November 13; published 2019 December 17

Abstract

The observation of radio, X-ray, and H_{α} emission from substellar objects indicates the presence of plasma regions and associated high-energy processes in their surrounding envelopes. This paper numerically simulates and characterizes critical velocity ionization (CVI), a potential ionization process, that can efficiently generate plasma as a result of neutral gas flows interacting with seed magnetized plasmas. By coupling a gas–magnetohydrodynamic (MHD) interactions code (to simulate the ionization mechanism) with a substellar global circulation model (to provide the required gas flows), we quantify the spatial extent of the resulting plasma regions, their degree of ionization, and their lifetime for a typical substellar atmosphere. It is found that the typical average ionization fraction reached at equilibrium (where the ionization and recombination rates are equal and opposite) ranges from 10^{-5} to 10^{-8} , at pressures between 10^{-1} and 10^{-3} bar, with a trend of increasing ionization fraction with decreasing atmospheric pressure. The ionization fractions reached as a result of CVI are sufficient to allow magnetic fields to couple to gas flows in the atmosphere.

Unified Astronomy Thesaurus concepts: [Magnetohydrodynamics \(1964\)](#); [Ionization \(2068\)](#); [Brown dwarfs \(185\)](#); [Extrasolar gas giants \(509\)](#); [Astrophysical fluid dynamics \(101\)](#)

1. Introduction

As well as emitting in the near-IR, substellar objects exhibit radio (e.g., Williams et al. 2015, 2017; Route & Wolszczan 2016), X-ray (e.g., Audard et al. 2007; Berger et al. 2010), and optical H_{α} (e.g., Schmidt et al. 2007; Pineda et al. 2016) emission. Despite their relatively low atmospheric temperatures, such emission indicates the presence of plasma and the associated high-energy processes in their surrounding envelopes. Several ionization processes occur in substellar atmospheres that generate regions of plasma, giving a source of the energetic, nonthermal processes required to generate the observed emission, including, thermal ionization (Rodríguez-Barrera et al. 2015), lightning discharges (Helling et al. 2013), cosmic-ray ionization (Rimmer & Helling 2013), photoionization (Rodríguez-Barrera et al. 2018), turbulence-induced dust–dust collisions (Helling et al. 2011), and critical velocity ionization (CVI; Stark et al. 2013).

In substellar atmospheres, thermal ionization could generate plasmas with degrees of ionization $f_e \approx 10^{-7}$, for at least some portion of the atmosphere, for pressures in the range $p_{\text{gas}} \approx 10^{-4}$ –10 bar. The degree of thermal ionization is strongly dependent on the effective temperature, the metallicity, and the log g of the object in question; the atmospheric volume fraction (at these pressures) that reaches this ionization fraction can increase from 10^{-3} to 1 by increasing the effective temperature from $T_{\text{eff}} \approx 1200$ to 3000 K (Rodríguez-Barrera et al. 2015). Triboelectric charging of dust cloud particles can lead to the buildup of strong electric fields, resulting in the large-scale electrical breakdown of the substellar atmospheric gas (Helling et al. 2013), including microscale intergrain breakdown (Helling et al. 2011). Within cloud regions ($p_{\text{gas}} \approx 10^{-5}$ –1 bar), such

electrical discharges could yield local degrees of ionization of about 10^{-1} (Beyer & Shevelko 2003; Guo et al. 2009), instantaneously enhancing the local plasma density. In substellar atmospheres, a lightning strike can have characteristic length scales of ≈ 0.5 –4 km, affecting atmospheric volumes of the order of 10^4 – 10^{10} m³ (Bailey et al. 2014). Cosmic-ray ionization can significantly enhance the degree of ionization for atmospheric pressures, $p_{\text{gas}} < 10^{-2}$. For giant gas planets, it is expected that cosmic-ray bombardment may create a weakly ionized plasma ($f_e \gtrsim 10^{-8}$) in the upper atmospheres of giant gas planets, where $p_{\text{gas}} < 10^{-8}$ (Rimmer & Helling 2013). Furthermore, photoionization by Lyman continuum radiation significantly increases the degree of ionization in the upper atmosphere, creating a shell of ionized material that can interact with the ambient magnetic field potentially leading to chromospheric activity and non-thermal emission (Rodríguez-Barrera et al. 2018).

CVI (also known as Alfvén ionization) is a process whereby a constant stream of neutral gas impinges on a low-density seed magnetized plasma (provided by e.g., cosmic rays, thermal ionization, etc.) (Alfvén 1960). The inflowing neutral atoms collide with and scatter the plasma ions, leaving behind a significant charge imbalance that accelerates electrons to energies sufficient to ionize the local gas via electron–neutral impact ionization. The critical ingredients for CVI include an initial, low-density magnetized seed plasma and a neutral gas flow that reaches a critical threshold speed. In substellar atmospheres, CVI can produce degrees of ionization ranging from $\approx 10^{-6}$ to 1, and is expected to be most effective where $p_{\text{gas}} \approx 10^{-5}$ – 10^{-15} bar, where flow speeds are sufficiently high, $\approx \mathcal{O}(1$ –10 km s^{−1}) (Stark et al. 2013). However, to fully characterize CVI in substellar atmospheres and to determine the distribution and spatial extent of the generated plasma regions, including their degree of ionization as a function of position, the role of the global circulatory system and the resulting atmospheric flows must be investigated.

The aim of this paper is to simulate CVI in substellar atmospheres to quantify the spatial extent of the resulting plasma regions, their degree of ionization, and their lifetime for a typical substellar atmosphere. This paper presents the novel coupling of a gas–magnetohydrodynamics interactions code (GMIC) with a substellar global circulation model (GCM) to investigate the impact of CVI on substellar environments, for the first time. In Section 2 a fluid description of CVI is outlined, describing Glasgow’s GMIC that simulates the CVI process. Section 3 describes the GCM for substellar atmospheres and the nature of the example atmosphere used here. Section 4 discusses the integration of GMIC with the GCM, quantifying the resulting plasma density, degree of ionization and the spatial extent of the plasma regions. In Section 5 we investigate the lifetime of the generated plasma by incorporating recombination rates into the model to find the conditions for ionization balance in the atmosphere.

2. A Fluid Description of CVI

CVI is a mechanism whereby the kinetic energy of the bulk motion of a neutral gas (with respect to a stationary seed plasma) perpendicular to an ambient magnetic field can be exploited to ionize the gas. The mechanism proceeds by first creating electric fields from the stochastic displacement of ions through elastic collisions with the neutral flow and then by the acceleration of the exposed free electrons across this newly created potential difference. These energetic electrons can excite and ionize neutral atoms through inelastic collisions, generating atmospheric plasma regions. CVI requires the presence of a small seed plasma and a magnetic field of sufficient strength to magnetize the electrons (i.e., of sufficient strength to reduce the Larmor radius of the electrons to less than the collisional scale length). Magnetized electrons are necessary for CVI because localized electrons are required to generate the ionization field (Wilson & Diver 2016). These constraints have previously shown to be satisfied extremely readily in brown dwarf atmospheres (Stark et al. 2013; Wilson & Diver 2017). The mechanism is always capable of generating nonthermal electrons, but only up to or slightly beyond the kinetic energy of the flow (MacLachlan et al. 2009). As such, no ionization is possible unless the neutral flow, in the frame of the stationary plasma, exceeds a “critical” speed, v_c , in the perpendicular-to-magnetic field direction; this speed is given by

$$v_c = \sqrt{\frac{2E_i}{m_g}}, \quad (1)$$

where E_i is the ionization energy, and m_g is the mass of the neutral atom (or molecule). Critical velocities for atoms range from around $\approx 5 \text{ km s}^{-1}$ for large-mass, low first-ionization potential elements to $\approx 50 \text{ km s}^{-1}$ for atomic hydrogen. More massive molecules can have lower critical velocities, making flows with a rich molecule mixture susceptible to CVI. Molecules with larger masses and approximately the same ionization potentials have substantially lower critical velocities than atoms. This velocity requirement, although falling below the sound speed for many objects (such as the Sun) or predicted wind speeds in substellar objects, means only reasonably energetic fluid motions will result in any CVI taking place.

This description of CVI is in terms of particle–particle interactions, which occur at sub-Debye length scales and on sub-Larmor period timescales; however, in contrast, the fluid flows evolve at the much slower hydrodynamical timescales. Wilson & Diver (2017) present an approach toward calculating CVI rates from fluid parameters in coupled MHD–gas simulations, we shall briefly lay out this approach.

As CVI proceeds, the kinetic energy of the neutral fluid flow is harnessed by plasma processes to effect a change in the internal energy state of the fluid, causing ionization when that change is optimal. Conservation of energy means that the relative flow velocities are reduced by an equal amount. Once the relative velocity between charged and neutral fluids has fallen below v_c , then CVI can no longer proceed unless the fluid is once more accelerated above that critical threshold. This means for a given volume of gas with neutral gas density, ρ_g , we can define an available reservoir of energy density available, E_{CVI} , given by the difference between the squares of the current velocity and the critical velocity,

$$E_{\text{CVI}} = \rho_g((v_g - v_p)^2 - v_c^2), \quad (2)$$

where v_g and v_p are the perpendicular-to-field component of the fluid velocity for the gas and seed plasma, respectively. Note that only the perpendicular component of the velocity matters, as the electrons are only magnetized in the plane perpendicular to the magnetic field. This reservoir is exhausted to ionize the neutral, the change in plasma density is given by

$$\dot{\rho}_p = m_g f E_{\text{CVI}} / E_i. \quad (3)$$

In Equation (3), we have introduced the parameter f which lies between 0 and 1 and has dimensions of inverse time making $\tau = 1/f$ the characteristic time over which the ionization occurs. f is the product of four numerical factors: the number of charge pockets that form in time t ; the average number of electrons in each charge pocket; the fraction of these electrons that reach ionization energies; and the probability that these electrons will ionize a neutral. A high f value means that any kinetic energy above the threshold speed v_c will quickly be converted to internal energy of the plasma, i.e., carry out ionization. This regime manifests as v_c becoming a saturation speed above which it becomes impossible to drive relative velocities. A low f value means that there is the ability for the fluid to sustain velocities in excess of v_c and the energy is extracted slowly. The ionization timescale dictates f as a decrease to the characteristic time, τ , will result in a corresponding decrease to the number of charge pockets that form in time τ (Wilson & Diver 2017).

Equation (3) simplifies the microscopic interactions into an average bulk response, involving only one tuneable parameter, f . Thus, the rate of change of plasma density can be obtained from a two-fluid description consistent with Wilson & Diver (2016, 2017): the GMIC approach. In essence, there is a feedback mechanism: fluid velocities can drive changes in ionization fraction not found elsewhere; changes in ionization fraction reduce fluid velocities in a very specific manner, and therefore CVI presents complex dynamical changes.

CVI has been studied in a large number of laboratory experiments that use $\mathbf{E} \times \mathbf{B}$ forces to drive plasma against a background gas in homo-polar devices (Fahleson 1961; Danielsson & Brenning 1975; Brenning 1981). In such

experiments, it is demonstrated that $f \approx 1$ and that v_c is the saturation speed. These results are also consistent with upper-atmosphere experiments such as those on Spacelab (Sasaki et al. 1986), the Space Shuttle mission STS-39 (Ahmadjian & Jennings 1995), and on board numerous sounding rockets (Stenbaek-Nielsen et al. 1990; Wescott et al. 1994).

In this work we assume there is a sufficiently high number density seed plasma, provided by other nonthermal ionization mechanisms, such as atmospheric discharges or cosmic rays or even by the low background population of thermal electrons. We also assume that there is a persistent global magnetic field, with a component normal to the body’s surface. Wilson & Diver (2016) showed that a magnetic field of 10^{-5} T (0.1 G) is more than strong enough to achieve CVI in even the most dense regions of substellar atmospheres.

3. Global Circulation Model

The model atmosphere used as a basis for the ionization calculations is that of the irradiated exoplanet HD 189733b, taken from radiative–hydrodynamical simulations described in Dobbs-Dixon & Agol (2013). The atmospheric dynamics seen in this model are characterized by supersonic winds propagating from the dayside to the nightside in broad equatorial jets (see also Showman et al. 2009). These high-velocity flows make HD 189733b (and similar objects) an ideal environment for CVI. Brown dwarfs are also seen somewhat frequently orbiting a companion star, so they could experience similar flows, driven by their parent body. For an isolated brown dwarf, the fast rotation speed drives equivalent fluid motions, as does the convective nature of their atmospheres, and km s^{-1} scale flows should be commonly encountered. Note that these gas atmospheric simulations only extend down to a pressure floor of 1.8×10^{-3} bar.

Figure 1 shows the gas density in the atmosphere of HD 189733b. The x and y axes denote a Cartesian grid for longitude and latitude, respectively, measured in degrees; the z -axis denotes the atmospheric pressure in bar. The substellar point is located at (180, 0). Note that the x axis is periodic, and the poles are the extremes of the y axis. Each consecutive slice in the positive z -direction corresponds to a factor of two reduction in atmospheric pressure and that the displayed region only contains approximately the top 1/3 of the total simulated atmosphere as below this level no CVI was observed. These pressure slices are used consistently for all similar figures.

Figure 2 shows the gas speed parallel to the surface. Clearly seen is the strong equatorial flow driven from the circumstellar point, as well as counterrotating flows of material at higher latitudes separated by a relatively narrow region of null velocity. The flows also grow stronger as the pressure reduces; only the deepest portion of the atmosphere is represented in these simulations, but this is a trend that will continue to higher altitudes. We assume that the seed magnetic field is orientated perpendicular to the surface, i.e., vertically; therefore, the perpendicular-to-field component of the fluid velocity is in the horizontal direction. Where this speed exceeds the critical velocity, there is expected to be CVI.

4. Incorporating CVI

Initially we calculate the maximum possible ionization that could be obtained from energy reservoir present for velocities above v_c using the fluid velocities taken from a snapshot of the

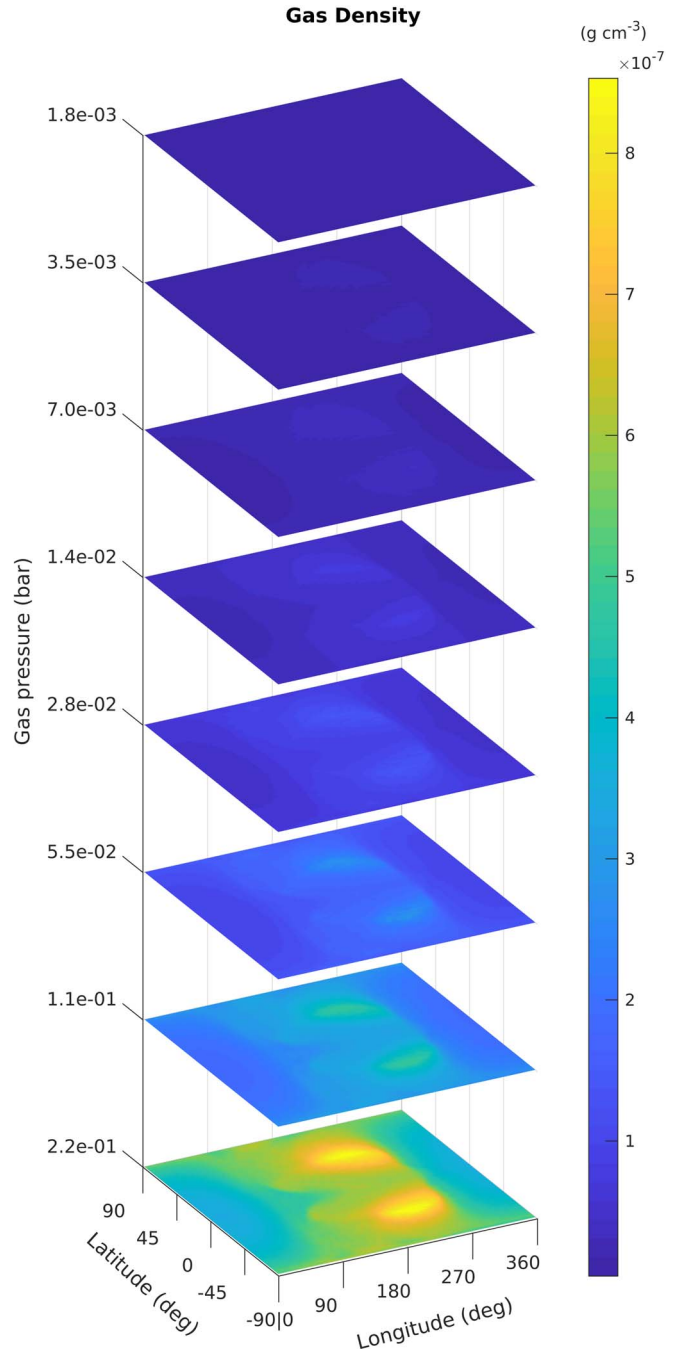


Figure 1. Density in g cm^{-3} for a series of isobaric slices through the atmosphere.

GCM simulation. HD 189733b has an atmosphere predominately composed of molecular hydrogen; however, it also contains an abundance of heavier elements and molecules such as H_2O , CO_2 , and CH_4 . These molecules have a larger mass and travel with the background flow and are therefore optimal for generating the stochastic potentials necessary for CVI. The critical velocity used is 5 km s^{-1} , in the middle of the expected relevant range $\mathcal{O}(1\text{--}10 \text{ km s}^{-1})$. Once electrons are produced they are able to interact with any atmospheric component, meaning that the most likely interactions occur with targets with the largest number densities. The most abundant atmospheric constituents are therefore the most likely to be ionized,

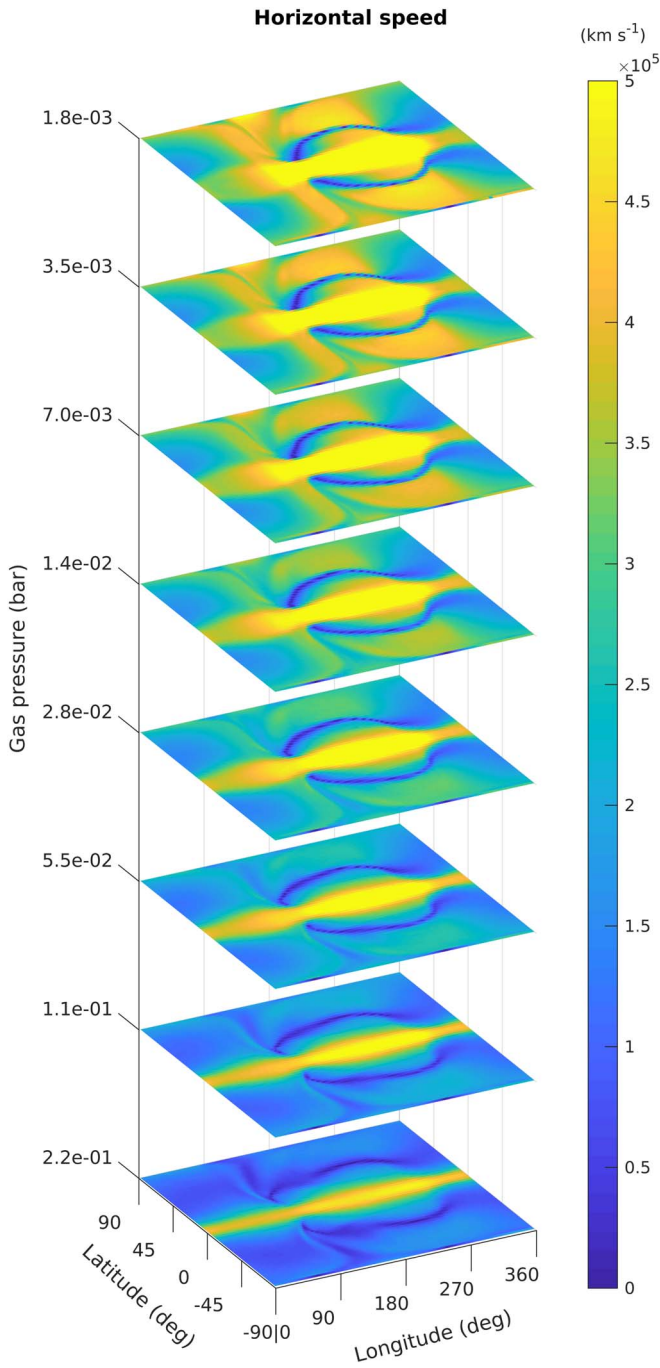


Figure 2. Horizontal speed in km s^{-1} i.e., the velocity moving in the plane of atmospheric slice. The color scale is saturated at 5 km s^{-1} to show the regions where the velocities exceeded a representative critical velocity.

as long as the electron energy distribution function contains electrons which exceed the ionization potential of the targets. Because hydrogen is the most abundant component, we use its first-ionization potential for E_i .

We compute the available kinetic energy reservoir (E_{CVI}) and the change in plasma density from Equations (2) and (3) and obtain a cell-by-cell change in plasma number density. This provides a ceiling for the maximum instantaneous production of plasma in this model atmosphere; this degree of ionization will reduce the velocity of the flow to v_c everywhere, at which point no further ionization can take place.

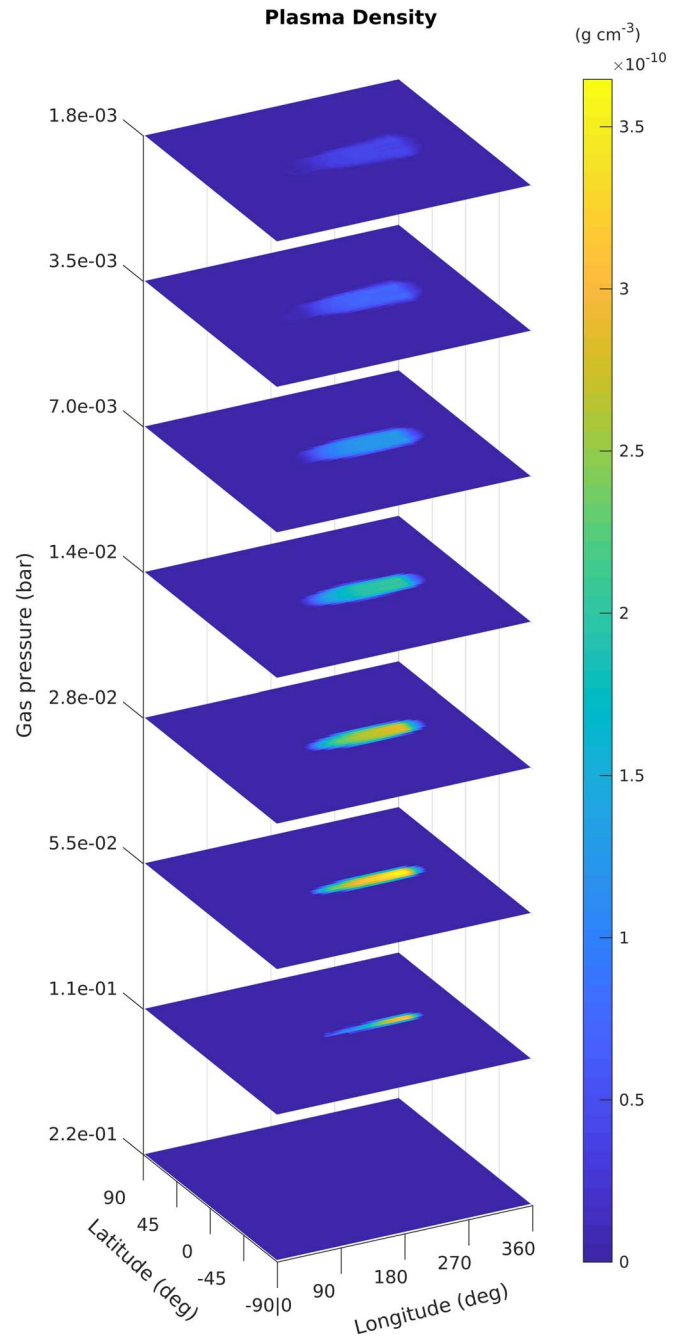


Figure 3. Plasma density in g cm^{-3} at a series of isobars above the surface. The highest plasma density is obtained at pressures between approximately 10^{-1} and 10^{-2} bar where plasma densities reach $10^{-10} \text{ g cm}^{-3}$. The plasma density is higher at lower depths, due to the increased gas density providing a larger kinetic energy reservoir, but this rapidly drops off to zero once atmospheric speeds drop below the critical velocity.

In previous dynamic simulations of CVI, this ionization has been spread out temporally by the ionization efficiency factor f . The case of $f = 1$ represents this situation, where all of the kinetic energy from the reservoir is exhausted before the fluid can react to the changing local fluid variables.

Figure 3 shows the distribution of this newly created plasma. The highest plasma densities are reached toward the bottom of the figure, at pressures around 10^{-1} bar. This is simply due to the larger gas densities and thus kinetic energy densities in these layers. Only approximately the top 1/3 of the spatial

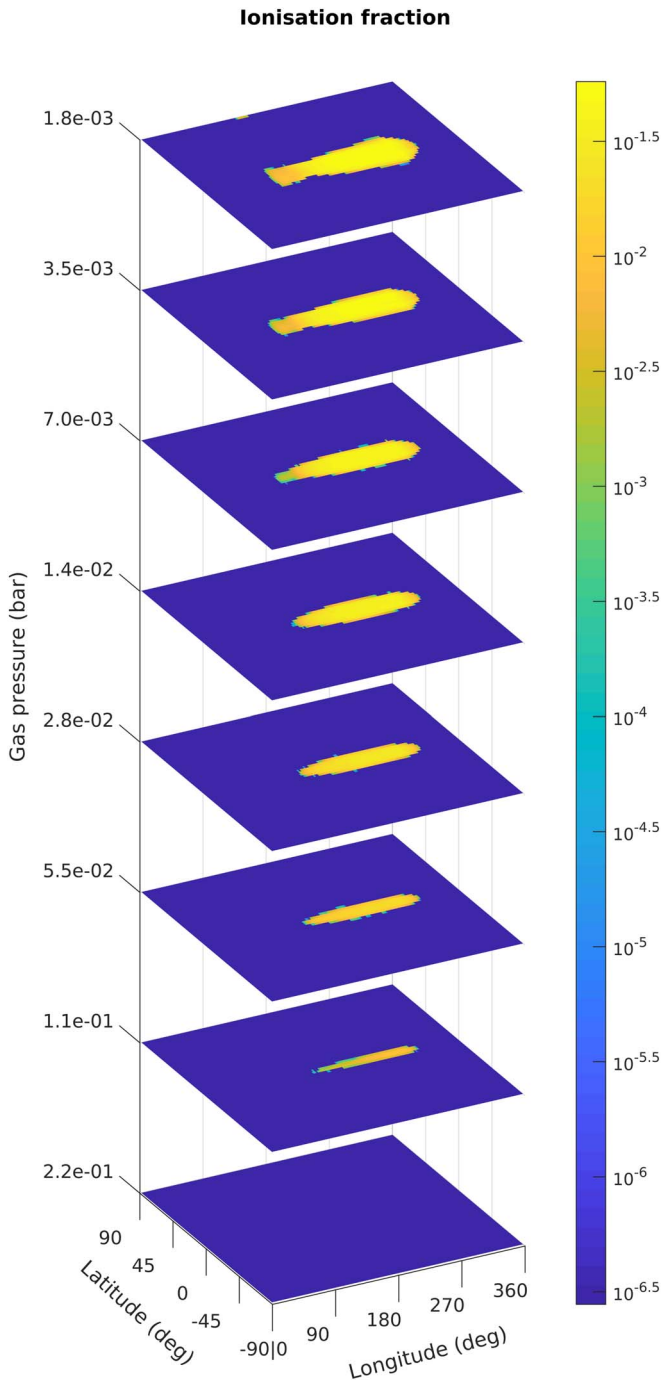


Figure 4. Common log of the ionization fraction after CVI has taken place (i.e., -2 corresponds to an ionization fraction of 0.01), for the same isobaric slices as previous figures. The peak ionization fraction reached is 0.15 for $v_c = 5 \text{ km s}^{-1}$ (and 0.061 for $v_c = 10 \text{ km s}^{-1}$). This maximum is found near the top of the atmosphere, where the density is lowest and flow velocities are highest.

extent of the GCM simulation is displayed; below the lowest level shown, the maximum velocities reached do not exceed the critical velocity.

Figure 4 shows the ionization fraction reached. The highest ionization fraction is reached toward the top of the simulated atmosphere at pressures $< 10^{-3}$ bar. The reason for this is the opposite trend as that shown in Figure 3: that change in plasma density is proportional to both the gas density and the squared relative velocity difference ($v_{\perp}^2 - v_c^2$), whereas the ionization

fraction, having been obtained by dividing by the density, is only dependent on the velocity difference. At high altitudes, where the higher velocities are more likely to exceed the critical velocity, there is more CVI. The ionization factor for these layers can reach up to approximately 0.15 (for $v_c = 5 \text{ km s}^{-1}$) at 10^{-3} bar, decreasing as you move to higher pressures.

While the CVI process is extremely fast, the source of these relative velocities must be established on the fluid timescale. Therefore, we choose to consider the competing mechanism of recombination.

5. Recombination

In this section, we address the long-term mean ionization equilibrium, a balance between CVI events and recombination. A crucial test is how long any CVI deviation from equilibrium will endure. Note that the low densities here mean that the recombination reaction rates are slow compared with CVI timescales. Hydrogen at 1200 K (approximately the atmospheric temperature) will have a negligible thermal ionization rate and a recombination rate coefficient $\kappa_r = 2.01 \times 10^{-12} \text{ cm}^3 \text{ s}^{-1}$ (Dere et al. 1997; Landi et al. 2012). Therefore, we can safely assume that the equilibrium ionization fraction is essentially zero. We will assume the thermal ionization rate remains zero in our perturbed system (there remains no thermal ionization energy level electrons). The net recombination rate is thus

$$\dot{n}_g = \kappa_r n_e n_i. \quad (4)$$

In a single species plasma, we assume $n_e = n_i$,

$$\dot{n}_g = \kappa_r n_e^2. \quad (5)$$

If we were to consider globally averaged plasma densities, then the lifetime of the plasma created by CVI would be measured in weeks. However, Figure 3 shows a pattern of highly localized plasma, collocated with the regions of highest velocity flows. Specific flow patterns in the atmosphere can increase the ability of the plasma to persist for long periods; as the recombination rate is proportional to plasma density squared, it is significantly easier for the average ionization fraction of the plasma to remain at an elevated level if the ionization is spread out over as much of the atmosphere as possible, rather than concentrated in a small volume. This necessitates a spatially resolved recombination simulation rather than basing an estimate on the recombination timescale on a global or otherwise large-scale averaged values for plasma density. Therefore, the time integration is done simultaneously in each fluid cell based on the local temperature and plasma density. For each timestep, we average the ionization fraction over each isobar.

Figure 4 demonstrates a feature of CVI: the total kinetic energy contained in a volume of flowing gas and the total energy required to fully ionize it are both directly proportional to the mass of the volume. In this way, the possible change in ionization fraction from a given relative velocity is independent of density. The peak plasma density is found at high pressure, where the gas density is maximum, but the highest ionization fractions are reached at lower pressures (greater altitudes). We can immediately predict that if two regions of the atmosphere, one with low gas density and one with high, are experiencing the same flow velocities, then they will experience the same change in ionization fraction. However, the higher gas density region will recombine significantly faster due to the higher plasma density, thus the higher recombination rate.

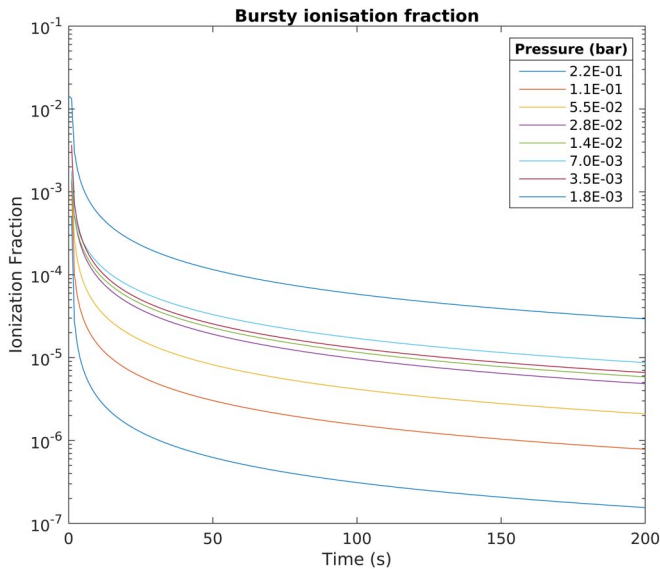


Figure 5. Common logarithm of the global average ionization fraction of each isobar as a function of time. Each line is the average taken over an entire pressure surface.

Figure 5 shows the average ionization fraction for a range of pressures, where we assume that all the ionization takes place in an initial burst. The first few seconds involve a rapid decrease in the ionization fraction, due to the density-squared dependency in recombination rates. Beyond this, the atmosphere sustains a prolonged period where the ionization fraction is maintained at somewhere between 10^{-5} and 10^{-6} in all but the deepest atmospheric layers.

If we were to assume the plasma was evenly spread over the entire atmosphere, the recombination would take tens of hours to decrease to the same average ionization fraction achieved in hundreds of seconds in Figure 5. The density-squared dependence of the recombination rate means that patterns such as shown in Figure 4 are comparatively short lived.

5.1. Time-dependent Ionization

We have already shown that more spatially distributed ionization results in any elevated ionization fraction recombining more slowly. The same is true if the ionization is spread temporally as well as spatially. A constant, low rate of ionization is optimal for maximum persistence of plasma in the atmosphere and therefore a steady mean ionization fraction. Figure 5 was based on a single burst of ionization at $t = 0$, using the atmospheric properties at that time. This was then followed by a long slow period of recombination. Figure 5 shows clearly that by far the most rapid period of recombination was immediately following the burst of CVI, with recombination slowing dramatically once the plasma density had dropped by 3–4 orders of magnitude, which equates to 6–8 orders of magnitude in recombination rate.

In CVI, electron acceleration occurs over the course of few Larmor periods (Wilson & Diver 2016). This is an extremely rapid process when compared with the fluid motions of the atmosphere. These same fluid motions are also what drive the conditions of CVI, and as such, the CVI rate itself evolves at the characteristic fluid time (seen in Equation (3)), τ , taken to be 10 hr (the fluid crossing timescale).

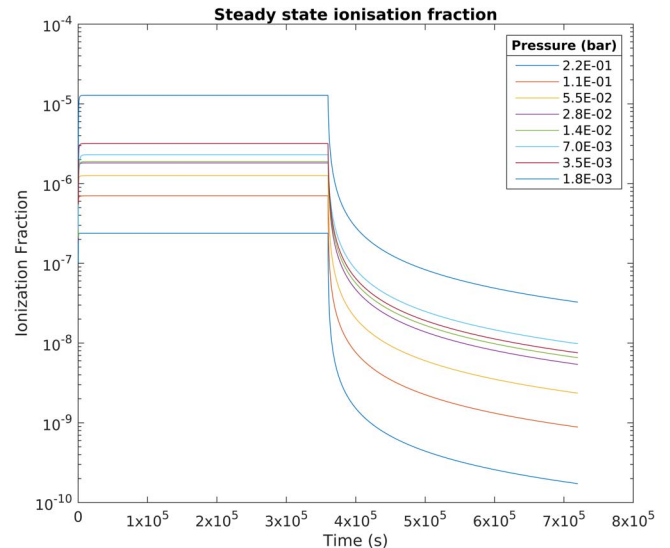


Figure 6. Evolution of the isobar-averaged ionization fraction. The ionization fraction quickly plateaus at an equilibrium position where the recombination rate and the ionization rate are equal and opposite.

The ionization caused by any relative velocities exceeding v_c is now gradual, rather than instantaneous. The ionization rate is kept constant until $t = \tau$ giving a value for f of $1/(10 \text{ hr})$; the total integrated ionization over τ is exactly equal to the total ionization used as the initial condition in the bursty simulation (Figure 5). The hydrodynamics of the system drives flows that result in ionization via CVI and recombination proceeds via collisional processes. The net balance of these processes naturally leads to an equilibrium ionization fraction that varies throughout the atmosphere. Figure 6 shows the time dependence of the ionization fraction for this “steady-state” ionization balance. The simulation runs from $t = 0$ to $t = 2\tau$ with the ionization ending at $t = \tau$. This figure shows 3 distinct stages: a very rapid increase in plasma density up to an equilibrium lasting only a few tens of seconds; a steady-state equilibrium that lasts until the energy reservoir is exhausted at $t = \tau$; and a more gradual relaxation phase which is similar to that seen in the burst ionization scenario, except that the initial plasma density is lower and, as such, the recombination is slower. In Figure 6, this third phase is seen because the simulation was extended past $t = \tau$ to see the persistence of the plasma once there are no longer velocities exceeding v_c . Note that in a realistic atmosphere, the flows will be renewed continually over a timescale of approximately τ . The mean ionization fraction may vary moment to moment based on the evolution of the fluid dynamics, but the atmosphere never reaches a state where there are no velocities above v_c , and thus never enters this recombination phase.

The pressure averaged peak ionization fraction, computed to be $\approx 10^{-5}$, occurs in the highest simulated layers of the atmosphere. This peak is more than three orders of magnitude lower than the initial condition in the burst scenario. However, this ionization fraction is maintained at a constant level up to $t = \tau = 10 \text{ hr}$, whereas in the burst case the ionization fraction had fallen below this 10^{-5} level after a few minutes and by 10 hr the plasma was almost nonexistent. We also reiterate that the value of τ is chosen because it is the expected time it would take for the flows to be replenished. This ionization fraction is more than sufficient for the magnetic field to be advected with the flows (i.e., has a magnetic Reynolds number > 1). The

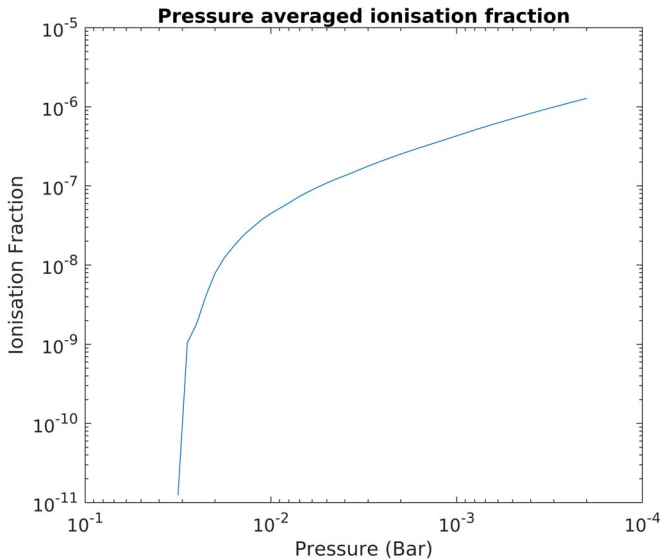


Figure 7. Average ionization fraction at ionization equilibrium as a function of gas pressure. There is a dramatic increase in the equilibrium ionization fraction as you move up the atmosphere. The trend suggests even higher ionization fractions would be present above our pressure ceiling.

ability for the average ionization fraction to be much higher in a steady-state scenario is due to the dependence of the recombination rate on the density squared; this allows the same CVI energy reservoir to provide more optimistic predictions on the abundance of ions in substellar atmospheres. If this energy reservoir is continually replenished, then this equilibrium ionization fraction is sustainable.

The choice of $\tau = 10$ hr represents an order of magnitude estimate of the crossing time (the time taken for typical flow speeds to circle the atmosphere). Because the recombination rate is proportional to the plasma density squared, then the equilibrium position must be proportional to $\tau^{-1/2}$. In this case, even if the value for τ is an order of magnitude higher (≈ 100 hr), the equilibrium ionization fraction will only be lowered by a factor of $\sqrt{10}$. This still clearly puts the ionization fraction within the range necessary to couple the magnetic field to the fluid motion.

Figure 7 shows the steady-state equilibrium ionization fraction as a function of gas pressure. There is clearly a dramatic trend in increasing ionization fraction with decreasing pressure as we look higher in the atmosphere. This increase comes as result of two aspects of the atmosphere: the typical flow velocities (both predicted and simulated) increase with decreasing pressure and the typical densities decrease with decreasing pressure. Both factors lead to a higher mean ionization fraction.

In addition, we draw attention to the fact that the GCM only extends down to $\approx 1.8 \times 10^{-3}$ bar. Models of the atmosphere of these substellar objects frequently extend to 10^{-10} bar and lower (Helling & Casewell 2014), we would expect the ionization fraction capable of being reached by CVI alone to be significantly higher at these pressures. As the level of ionization increases, the magnetic Reynolds number increases and the magnetic field begins to play more of a role in the large-scale fluid dynamics. To properly capture the dynamic, ionized atmosphere a study of these lower pressures would require using an MHD fluid model (as opposed to gas model used here), as well as the feedback loop of a full GMIC

simulation: where ionization interacts with both the magnetic field (via MHD) and feeds back to the flow velocities, rather than retroactively calculating the ionization rates in isolation.

6. Conclusions

This paper presents the novel coupling of a GMIC with a substellar GCM to investigate the impact of CVI on substellar environments for the first time. In global hydrodynamical models of brown dwarf and extrasolar planetary atmospheres, there exists flows of comparable magnitude to the critical velocity, the velocity at which bulk kinetic energy can cause CVI in the presence of a perpendicularly oriented magnetic field and a small seed plasma. This energy reservoir is exploited to produce a degree of ionization in said atmosphere that is inconsistent with a thermal equilibrium ionization fraction. The total plasma density produced, and its spatial distribution, was calculated for global radiative hydrodynamic simulations of extrasolar planet HD 189733b (Dobbs-Dixon & Agol 2013); the pressure averaged peak ionization fraction was found to lie between 10^{-4} and 10^{-2} , depending on the atmospheric pressure, but the highly localized distribution of plasma resulted in some regions of the atmosphere reaching a peak ionization fraction of 0.15.

Ionization has a competing mechanism: recombination. We show that if the plasma is evenly distributed throughout the atmosphere it would be long lived. However, the plasma created from CVI is not evenly distributed but is concentrated in volumes of the atmosphere which contained particularly high flow velocities. The density-squared dependence of recombination rate means where the plasma density is highest the recombination rate, assuming equivalent temperatures, is also highest and as such it is much easier to maintain a small amount of plasma spread over a large atmospheric volume than a large plasma density in small, localized volumes.

By solving a set of differential equations for the time-dependent plasma density from the recombination of the plasma in the three-dimensional volume, with the initial conditions in plasma density calculated from the flow velocities, we show the evolution of the nonequilibrium plasma density. Due to the heavily localized nature of the CVI plasma, only appearing where velocities were particularly high, this results in it recombining significantly faster in this scenario than if we were take a zero-dimensional approximation.

The velocities found in the lower levels of the atmosphere are of lower magnitude compared with higher up, with only extremely small regions of atmosphere being suitable for CVI. This concentration of the ionization into a few small areas means the plasma is extremely short lived when compared with the upper atmospheric layers where, although the plasma density is initially much lower due to the initial gas density being lower, the flows exceeded the critical velocity for a much higher fraction of the volume. As a result, ionization fraction, which for CVI is independent of the gas density, becomes a much more useful measure of the plasma conditions.

Kinetic energy extracted for CVI is removed from the flows. There is a dynamical feedback mechanism between the hydrodynamics that drive the flows, and the CVI which acts to reduce them. In the modeling done here this feedback could not be incorporated because only a snapshot of the stellar flows was used. Instead the ionization rate was controlled by choosing $\tau = 10$ hr, the approximate fluid crossing time, and thus the approximate time at which flows can evolve. In this manner the ionization is spread

out in time (as opposed to all occurring at $t=0$). This results in a reduced peak ionization fraction but allows the peak ionization fraction to be maintained for a longer period of time. This is more representative of how the ionization is expected to behave, because the same flows that are driving the fluid evolution of the atmosphere are controlling the conditions which result in CVI.

The typical equilibrium ionization fraction reached in this way ranges from 10^{-5} to 10^{-8} , at pressures between 10^{-3} and 10^{-1} bar. These are extremely promising results, implying high (>1) magnetic Reynolds number plasmas are possible to obtain with only the nonthermal electrons from CVI and no additional ionization mechanisms. The plasma densities are easily high enough to allow magnetic fields to be advected by gas motion. In addition, we show a trend of increasing ionization fraction with increasing height in the atmosphere. This contrasts with e.g., thermal ionization where significant ionization only occurs in the deepest layers, where the temperatures are highest. The simulations reported here are focused on relatively deep layers of the atmosphere; we would expect even higher ionization fractions at lower atmospheric pressures in a more comprehensive model.

While we do consider the finite reservoir of energy present in flows above the critical velocity, we are neglecting the dynamical feedback that CVI causes, where reducing flow speeds anywhere can affect the global circulation and where increasing the ionization fraction makes MHD behavior relevant with the flows being coupled to the field for at least some of the atmosphere. This dynamical feedback, fully incorporated using GMIC (Wilson & Diver 2017), is the focus of future work.

D.A.D. and A.D.W. are grateful for funding from EPSRC via grant No. EP/N018117/1. C.R.S. is grateful for funding from the Carnegie Trust for the Universities of Scotland via research incentive grant No. RIG007788. A.D.W. gratefully acknowledges the support of NVIDIA Corporation with the donation of a Titan Xp GPU used in this research. Data used in this project are available at <https://doi.org/10.5525/gla.researchdata.910>.

ORCID iDs

A. D. Wilson  <https://orcid.org/0000-0003-0820-8159>

References

- Ahmadjian, M., & Jennings, D. E. 1995, *JSpRo*, **32**, 507
 Alfvén, H. 1960, *RvMP*, **32**, 710
 Audard, M., Osten, R., Brown, A., et al. 2007, *A&A*, 471, 3
 Bailey, R. L., Helling, C., Hodosán, G., Bilger, C., & Stark, C. R. 2014, *ApJ*, **784**, 43
 Berger, E., Basri, G., Fleming, T., et al. 2010, *ApJ*, **709**, 332
 Beyer, H. F., & Shevelko, V. P. 2003, *Introduction to Physics of Highly Charged Ions* (Boca Raton, FL: CRC Press)
 Brenning, N. 1981, *PIPh*, **23**, 967
 Danielsson, L., & Brenning, N. 1975, *PhFI*, **18**, 661
 Dere, K., Landi, E., Mason, H., Fossi, B. M., & Young, P. 1997, *A&AS*, **125**, 149
 Dobbs-Dixon, I., & Agol, E. 2013, *MNRAS*, **435**, 3159
 Fahlson, U. V. 1961, *PhFI*, **4**, 123
 Guo, Y.-X., Yuan, P., Shen, X.-Z., & Wang, J. 2009, *PhyS*, **80**, 035901
 Helling, C., & Casewell, S. 2014, *A&ARv*, **22**, 80
 Helling, C., Jardine, M., & Mokler, F. 2011, *ApJ*, **737**, 38
 Helling, C., Jardine, M., Stark, C., & Diver, D. 2013, *ApJ*, **767**, 136
 Helling, C., Jardine, M., Witte, S., & Diver, D. A. 2011, *ApJ*, **727**, 4
 Landi, E., Del Zanna, G., Young, P., Dere, K., & Mason, H. 2012, *ApJ*, **744**, 99
 MacLachlan, C. S., Diver, D. A., & Potts, H. E. 2009, *NJPh*, **11**, 063001
 Pineda, J. S., Hallinan, G., Kirkpatrick, J. D., et al. 2016, *ApJ*, **826**, 73
 Rimmer, P. B., & Helling, C. 2013, *ApJ*, **774**, 108
 Rodríguez-Barrera, M. I., Helling, C., Stark, C. R., & Rice, A. M. 2015, *MNRAS*, **454**, 3977
 Rodríguez-Barrera, M. I., Helling, C., & Wood, K. 2018, *A&A*, **618**, A107
 Route, M., & Wolszczan, A. 2016, *ApJL*, **821**, L21
 Sasaki, S., Kawashima, N., Kuriki, K., et al. 1986, *GeoRL*, **13**, 434
 Schmidt, S. J., Cruz, K. L., Bongiorno, B. J., Liebert, J., & Reid, I. N. 2007, *AJ*, **133**, 2258
 Showman, A. P., Fortney, J. J., Lian, Y., et al. 2009, *ApJ*, **699**, 564
 Stark, C. R., Helling, C., Diver, D. A., & Rimmer, P. B. 2013, *ApJ*, **776**, 11
 Stenbaek-Nielsen, H., Wescott, E., Haerendel, G., & Valenzuela, A. 1990, *GeoRL*, **17**, 1601
 Wescott, E., Stenbaek-Nielsen, H., Hampton, D., & Delamere, P. 1994, *JGR*, **99**, 2145
 Williams, P. K. G., Casewell, S. L., Stark, C. R., et al. 2015, *ApJ*, **815**, 64
 Williams, P. K. G., Gizis, J. E., & Berger, E. 2017, *ApJ*, **834**, 117
 Wilson, A. D., & Diver, D. 2016, *PhPI*, **23**, 072117
 Wilson, A. D., & Diver, D. A. 2017, *PhPI*, **24**, 092112